

# Advantages of internal reference in holographic shaping ps supercontinuum pulses through multimode optical fibers

LINDA PISCOPO<sup>1,2,\*</sup>, LIAM COLLARD<sup>1,3</sup>, FILIPPO PISANO<sup>1,4</sup>, ANTONIO BALENA<sup>1</sup>, MASSIMO DE VITTORIO<sup>1,2,3,\*</sup> AND FERRUCCIO PISANELLO<sup>1,3,\*</sup>

<sup>1</sup>*Istituto Italiano di Tecnologia, Center for Biomolecular Nanotechnologies, Arnesano, LE 73010, Italy*

<sup>2</sup>*Dipartimento di Ingegneria Dell'Innovazione, Università del Salento, Lecce 73100, Italy*

<sup>3</sup>*RAISE Ecosystem, Genova, Italy*

<sup>4</sup>*Department of Physics and Astronomy "G. Galilei", University of Padova, Via Marzolo 8, 35131, Padova, Italy*

\* Corresponding authors: [linda.piscopo@iit.it](mailto:linda.piscopo@iit.it), [massimo.devittorio@iit.it](mailto:massimo.devittorio@iit.it) [ferruccio.pisanello@iit.it](mailto:ferruccio.pisanello@iit.it)

**Abstract:** The use of wavefront shaping has found extensive application to develop ultra-thin endoscopic techniques based on multimode optical fibers (MMF), leveraging on the ability to control modal interference at the fiber's distal end. Although several techniques have been developed to achieve MMF-based laser-scanning imaging, the use of short laser pulses is still a challenging application. This is due to the intrinsic delay and temporal broadening introduced by the fiber itself, which requires additional compensation optics on the reference beam during the calibration procedure. Here we combine the use of a supercontinuum laser and an internal reference-based wavefront shaping system to produce focused spot scanning in multiple planes at the output of a step-index multimode fiber, without the requirement of a delay line or pulse pre-compensation. We benchmarked the performances of internal vs external reference during calibration, finding that the use of an internal reference grants better focusing efficiency. The system was characterized at different wavelengths, showcasing the wavelength resiliency of the different parameters. Lastly, the scanning of focal planes beyond the fiber facet was achieved by exploiting the chromato-axial memory effect.

## 1. Introduction

Neural tissue endoscopy has emerged as a promising tool for studying local microcircuitry[1] in deep brain regions, enabling cell type-specific mapping of neural activity[2], observation of sub-cellular structures[3], and investigation of related physiological and pathological states[4], in a minimally invasive fashion. Fiber bundles[5–7] and graded index (GRIN) lenses[8] are greatly supporting neuroscientists, facilitating imaging of sub-cortical structures. However, the demand for ultra-compact implant cross-sections has driven the advancement of endoscopic techniques based on multimode optical fibers (MMFs). MMFs can indeed carry a wealth of information with thousands of modes guided within a 50  $\mu\text{m}$  diameter core [9]. Despite guided modes are mixed into a seemingly random speckle pattern at the output facet[10], the phenomenon is a deterministic process that can be controlled by employing optimization algorithms that leverage the estimate the fiber transmission matrix (TM). These methods include

phase modulation techniques based on spatial light modulators (SLMs) or digital micromirror devices (DMDs)[11–13]: the TM is assessed by iterative interferometric measures, detecting the interferogram between a varying-phase hologram propagated through the MMF[14] (the probe beam) and a fixed-phase reference that can be external or internal to the MMF. Interesting alternatives are represented by digital phase conjugation[15] and phase retrieval[16] algorithms with the advantage of not relying on interferometric measurement based on references but requiring complex alignments or leading to lower light confinement in the focused spots. Another reference-free class of techniques that have emerged over the years are based on machine learning algorithms[17–19]. These techniques may be advantageous due to their resilience to dynamic perturbation of the TM[20,21], such as bending and temperature but demand extensive amounts of data[22]. These paradigms pushed the performances of MMF endoscopy, harnessing the speckles to structure output light and obtain diffraction-limited raster-scanning imaging[23], super-resolution nanomicroscopy[24], and time of flight measurements for reconstructing three-dimensional images several centimeters beyond the fiber tip[25].

A frontier topic is represented by the translation to the realm of MMF endoscopy of a set of microscopic techniques requiring the use of visible or near-infrared light excitation short pulses including two-photon imaging[26], fluorescence lifetime imaging (FLIM)[27] and coherent anti-stokes Raman spectroscopy (CARS)[28,29]. These applications require broadband wavelength tunability to fully enable the operator to optimize the excitation for the employed fluorescent reporters (for instance for FLIM), or to better exploit non-linear phenomena (such as 2P absorption or CARS). Aside from the spectral requirements, the use of wavelength-tunable short pulses sources adds another level of complexity, since the short pulses of the light source ( $\sim 100$  fs) guided into the MMF undergo temporal broadenings due to modal dispersion. This affects the interferometric measurements required to estimate the TM by reducing the probability of a temporal overlap across the output measurement plane. In fact, when the radiation is pulsed, the interference of the internal modes with the reference beam at the measurement plane can occur only if the internal modes of the fiber overlap in space and time with the reference pulse. This caveat can be addressed by adding an adjustable delay line on the external reference beam, to select only the modes with similar group velocities directly during the interferogram measurement[28,30]. Nevertheless, in addition to complicating the optical path, this method introduces a temporal overlap between the probe and reference pulses that remains only partial owing to their distinct temporal broadening, thereby diminishing the overall efficiency of the process. An alternative strategy lies in temporal focusing, necessitating the utilization of temporal wavefront shaping on a beam that has already undergone spatial shaping. However, this method demands extended computational time and additional optical components.[31].

Here we describe how the combination of an internal reference with a supercontinuum light source can be employed to obtain volumetric raster scanning of a picosecond-pulsed beam at multiple wavelengths generated by a photonic crystal fiber. The internal reference undergoes similar dispersion and delaying effects affecting the probe beam, avoiding the group-velocity filtering that instead characterizes systems based on a delayed external reference. This removes the need for an external adaptable delay line, streamlines the optical setup, and enhances focusing efficiency within the focused spot but does not allow control of the temporal profile of

the pulse propagating inside the fiber. Tiny variations (1 nm) of the source wavelength enable the chromato-axial memory effect to move the raster-scanning plane along the fiber axis, while multi-wavelength calibrations warrant the use of the system in multiple spectral ranges.

## 2. Results

### 2.1 Operating principle and optical path

To properly shape the light intensity pattern at the output of a MMF, a preliminary calibration step[32] is required. The calibration procedure consists of measuring the interference patterns  $I_{probe}^{ref}(x_{i_1}^{in}, y_{i_2}^{in}, \phi_i)$  between several probe beams  $B_{probe}(x_{i_1}^{in}, y_{i_2}^{in}, \phi_i)$  transmitted sequentially through the MMF and a reference beam  $B_{ref}(x_{ref}, y_{ref})$ , where  $(x_{i_1}^{in}, y_{i_2}^{in})$  identifies different positions of the probe beam at the fiber input, hereafter referred to as “external spatial modes”.  $B_{ref}(x_{ref}, y_{ref})$  is instead injected at a fixed location (**Figure 1A**, “internal reference”) at the input facet or skips the fiber to implement an “external reference” configuration, used for comparison (**Figure 1B**). For each  $(x_{i_1}^{in}, y_{i_2}^{in})$  input position, the phase of the probe beam  $\phi_i$  is varied between 0 and  $2\pi$ . Then, an optimization algorithm operates on the recorded  $I_{probe}^{ref}(x_{i_1}^{in}, y_{i_2}^{in}, \phi_i)$  to identify the optimum  $\phi_i$  value that generates constructive interference at a target output position at the distal fiber facet  $(x_{j_1}^{out}, y_{j_2}^{out})$  (see planes definitions in **Figure 1A**). This allows identifying the phase wavefront that needs to be injected in the MMF input to obtain a diffraction-limited focused spot at the output of the MMF[33]. During the calibration procedure, each of the external spatial modes  $(x_{i_1}^{in}, y_{i_2}^{in})$  is decomposed into the internal guided modes of the MMF. For pulsed coherent light, the interference of the internal modes with the reference beam at the output facet can occur only if the internal modes of the fiber overlap in space and time with the reference pulse. To compensate for this, methods using an external reference need an adjustable delay line that must be tuned to match the temporal delay arising from the group velocities of different modal subsets [34]. This, in turn, results in a more complex optical path, but also in a sub-optimal temporal overlap [30]. Indeed, the external reference and the probe beams undergo to different dispersions, resulting in a different pulse broadening and effective interference in a time window shorter than the broadened pulse of  $B_{probe}$  (**Figure 1B**). The use of an internal reference would instead allow  $B_{probe}$  and  $B_{ref}$  to experience similar modal dispersion inside the MMF (**Figure 1A**).

To test this hypothesis, we employed the optical setup depicted in **Figure 1C**, composed of three main sections: (i) a supercontinuum generation module, (ii) a wavelength selection block, and (iii) a phase modulation block. In the first block, a 785 nm fs-pulsed laser (TOPTICA FemtoFiber smart 780, pulse duration  $\sim 93$  fs) is expanded by lenses L1 (focal length  $f_{L1} = 75$  mm) and L2 ( $f_{L2} = 300$  mm) and then focused by Obj1 (0.5 NA, 20x, RMS20x-PF, Olympus) on the facet of a 12 cm-long photonic crystal fiber (PCF, NKTPhotonics, FemtoWHITE 800), using a  $\lambda/2$  waveplate to match the laser polarization with the principal polarization axis of the PCF. Due to the extreme confinement in the photonic crystal, the laser interacts non-linearly with the PCF core, broadening the laser spectrum. The pump laser wavelength was chosen to be larger than the zero-dispersion wavelength ( $\lambda_{zero} = 750$  nm) of the PCF to obtain a broader spectrum[35]. The supercontinuum beam generated by the PCF is collected by Obj2 (0.5 NA, 20x, RMS20x-PF, Olympus) and focused by an achromatic doublet L4 (AC-254-100-AB-ML,  $f_{L4} = 100$  mm) on the input slits of a monochromator (HORIBA, microHR,  $f_{\#MC} = 3.88$ ). The

achromatic doublet focal length was chosen to match the f-number of the monochromator ( $f/\#_{L4}=3.9$ ). The angularly dispersed output light, with a spectral dispersion on the slit plane of 5.25 nm/mm, was filtered with a slit and collimated with lens L5 ( $f_{L5} = 35$  mm). The filtered light was then routed towards a phase-only spatial light modulator (SLM, ODP512, Meadowlark Optics), using a  $\lambda/2$  waveplate to match the polarization of the collimated beam to the SLM modulation axis. After the waveplate, a beam expander, composed of the lenses L6 ( $f_{L6} = 25$  mm) and L7 ( $f_{L7} = 250$  mm), resized the beam to slightly overfill the SLM screen. The screen of the SLM was conjugated with the back focal plane of Obj3 (0.65 NA, 40x, AMEP4625, ThermoFisher) by a 4f system consisting of the lenses L8 ( $f_{L8} = 400$  mm) and L9 ( $f_{L9} = 200$  mm). Obj3 focused the modulated wavefront on the back facet of an MMF segment (0.22 NA, 50  $\mu$ m core diameter, Thorlabs FG050UGA). The MMF employed in the experiments was 50 mm in length, compatible with endoscopic applications in mouse brain imaging[1,36]. While propagating through the fiber, both  $B_{probe}$  and  $B_{ref}$  supercontinuum pulses experience modal dispersion, due to the different group velocities of the internal modes, with the fiber length having an impact on the resulting average temporal broadening of the pulse. The temporal difference  $\Delta\tau$  between the longer and the shortest optical path that a mode can follow inside the core can be estimated as  $\Delta\tau = \frac{NA^2L}{cn_{core}}$ , where NA is the numerical aperture of the fiber,  $L$  is its length,  $n_{core}$  is the core refractive index, and  $c$  is the speed of light in vacuum[25]. For the fibers used in this work  $NA = 0.22$ ,  $L = 50$  mm,  $n_{core} = 1.458$ , resulting in  $\Delta\tau = 5.5$  ps. The speckle patterns at the fiber output were collected by Obj4 (0.65 NA, 40x, RMS40X, Olympus) and imaged on a charged coupled device (CCD) by L11 ( $f = 125$  mm).

To generate the external spatial modes  $B_{probe}(x_{i_1}^{in}, y_{i_2}^{in}, \phi_i)$ , blazed phase gratings with different orientations were employed to define a 50 x 50 input matrix (**Figure 1A, left**), and for each four phase steps were tested ( $\phi_i = 0, \frac{\pi}{2}, \pi, \frac{3\pi}{2}$ ). The 2500 elements of the input matrix allow to generate a number of external spatial modes higher than the number of guided modes at each of the tested wavelengths ( $M = \frac{1}{2} \left( \frac{2\pi r}{\lambda} NA \right)^2$ ), a condition warranting to exploit the full modulational capabilities through MMFs. The reference beam  $B_{ref}(x_{ref}, y_{ref})$  was generated by an additional grating and focused on the MMF on a fixed  $(x_{ref}, y_{ref})$  position or directed toward a delay line for comparison. Before displaying on the SLM, the gratings were Fourier transformed and summed. For every  $(x_{i_1}^{in}, y_{i_2}^{in})$ , the optimal phase shift  $\phi_i^{opt}$  that gives the maximum intensity value for each pair of coordinates  $(x_{j_1}^{out}, y_{j_2}^{out})$  was stored. By summing the gratings generating  $B_{probe}(x_{i_1}^{in}, y_{i_2}^{in}, \phi_i^{opt})$  in the Fourier plane, the optimized input phase modulation masks (**green dashed box in Figure 1C**) are generated to scan the focused spots in each of  $(x_{j_1}^{out}, y_{j_2}^{out})$  of a 30 by 30 array on the output facet (**Figure 1A, center**).

In the following, the optical system and the described algorithm are first employed to benchmark the differences between using a pulsed laser with an internal or external reference and versus the case of a continuum wave laser. Later, the resiliency to wavelength and the implementation of the chromato-axial memory effect to generate three-dimensional raster scanning grids are analysed.

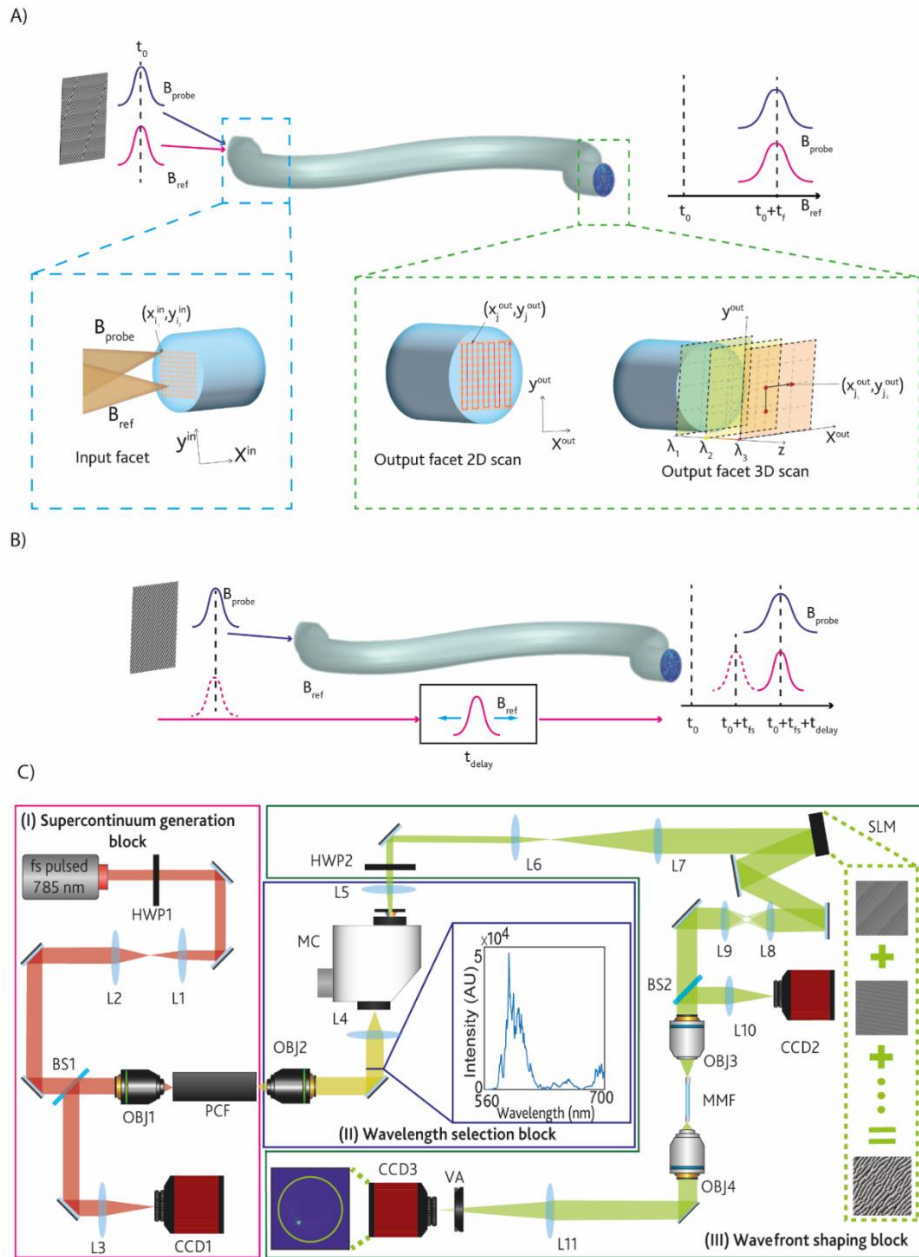


Fig.1.: Graphical representation of the working principle of the calibration algorithm for internal reference. The resultant scanning foci at the output of the multimode fiber are shown in the central panel. The possibility to tune the wavelengths allows moving the focused spot in the z-axes for a volumetric scan (right panel). B) Graphical representation of the working principle of the calibration algorithm for external reference based systems. C) Schematic representation of the optical setup, divided into three main blocks: (I) supercontinuum generation, (II) wavelength selection and (III) wavefront shaping. In (II) an example of supercontinuum spectrum in the visible range obtained with a polarization angle of  $45^\circ$  to the optical table and input coupled power of 46 mW is presented. Optical elements: HWP – half wave plate, L – lens, BS – beamsplitter, CCD – charged coupling device, OBJ – microscope objective, PCF – photonic crystal fiber, MC – monochromator, SLM – spatial light modulator, MMF – multimode fiber, VA – variable attenuator.

## 2.2 Focusing short pulses with internal reference

A focused spot scanning across the output facet obtained with the above-described system tuned at  $\lambda = 600$  nm is displayed in **supplementary video 1**, with a representative frame reported in the inset of **Figure 2A**. A beam waist ( $1/e^2$  of the maximum) estimation gave  $w_{int} = 4.28 \pm 1.18 \mu\text{m}$  (mean  $\pm$  standard deviation,  $n = 550$ ) over the entire scanning field, approaching the diffraction limit related to the fiber NA ( $\frac{1.22\lambda}{NA} = 3.32 \mu\text{m}$ ). The same characterization was performed with an external reference beam and produced a statistically indistinguishable average beam waist  $w_{ext} = 4.53 \pm 1.70 \mu\text{m}$  ( $p = 0.063$ , t-test, the delay line was optimized to give the highest fringes contrast in the interferometric calibration procedure). For comparison, a continuous wave (CW) laser at  $\lambda = 633$  nm in internal reference configuration gave  $w_{cw} = 3.13 \pm 0.70 \mu\text{m}$ . The statistical distribution of the obtained waists across the fiber core is reported by the histograms in **Figure 2A**.

For each  $(x_{j_1}^{out}, y_{j_2}^{out})$  on the output facet, the quality of the calibration process was estimated by calculating the focusing efficiency, defined as intensity in the focused spot divided by the intensity in the overall core of the fiber[12,14]:

$$FE(x^{out}, y^{out}) = \frac{\sum_{(j_1^2 + j_2^2) < w^2} I(x_{j_1}^{out}, y_{j_2}^{out})}{\sum_{(j_1^2 + j_2^2) < D^2} I(x_{j_1}^{out}, y_{j_2}^{out})} < 1,$$

where  $D = 50 \mu\text{m}$  is the fiber diameter. A relatively uniform FE was obtained across the facet (**Figure 2B, left**), with a slight decrease as a function of the distance from the core (green line in **Figure 2B, right**). Comparison with external reference data (blue line) shows a higher FE for the internal reference calibration, which is confirmed by the overall FE distribution reported in **Figure 2C**. In terms of average value, we obtained  $\langle FE_{int} \rangle = 0.22$  (standard deviation 0.04,  $n = 550$ ) for the internal reference and  $\langle FE_{ext} \rangle = 0.096$  (std 0.004,  $n = 550$ ) for delayed external reference, quantifying a  $\sim 2.3$  times increase. This difference can be explained by considering the temporal characteristic of the pulse duration before and after the MMF, which was measured using an autocorrelation technique implemented with a Michelson interferometer (**Figure 2D**). The pulse duration before the transmission through the fiber (which is also the pulse duration of the external reference) was estimated to be  $\tau_{ref} \sim 1.67 \pm 0.10$  ps, while the pulsed speckle pattern duration after the transmission through the fiber was found to be  $\tau_{probe} \sim 2.6 \pm 0.5$  ps. As a result, even if in the external reference scheme a delay line is employed to temporally synchronize the two pulses, the pulse transmitted through the MMF will be approximately 36% longer than the reference pulse (**Figure 2E**) and the interference will happen only in the overlapping portion of the pulses (see overlapping area in **Figure 2E**). This supports the hypothesis that an internal reference allows a better overlap of the probe and the reference pulses during calibration. However, a certain degree of mismatch persists also in the case of the internal reference, due to the low interferometric compatibility of guided modes that experience low or extreme delays with the internal reference. As a result, CW implementations achieve better FE performances, as shown by the comparative data reported in red **Figure 2B and C** ( $\lambda_{CW} = 633$  nm, internal reference,  $\langle FE_{CW} \rangle = 0.34$ , std 0.05,  $n = 550$ ).

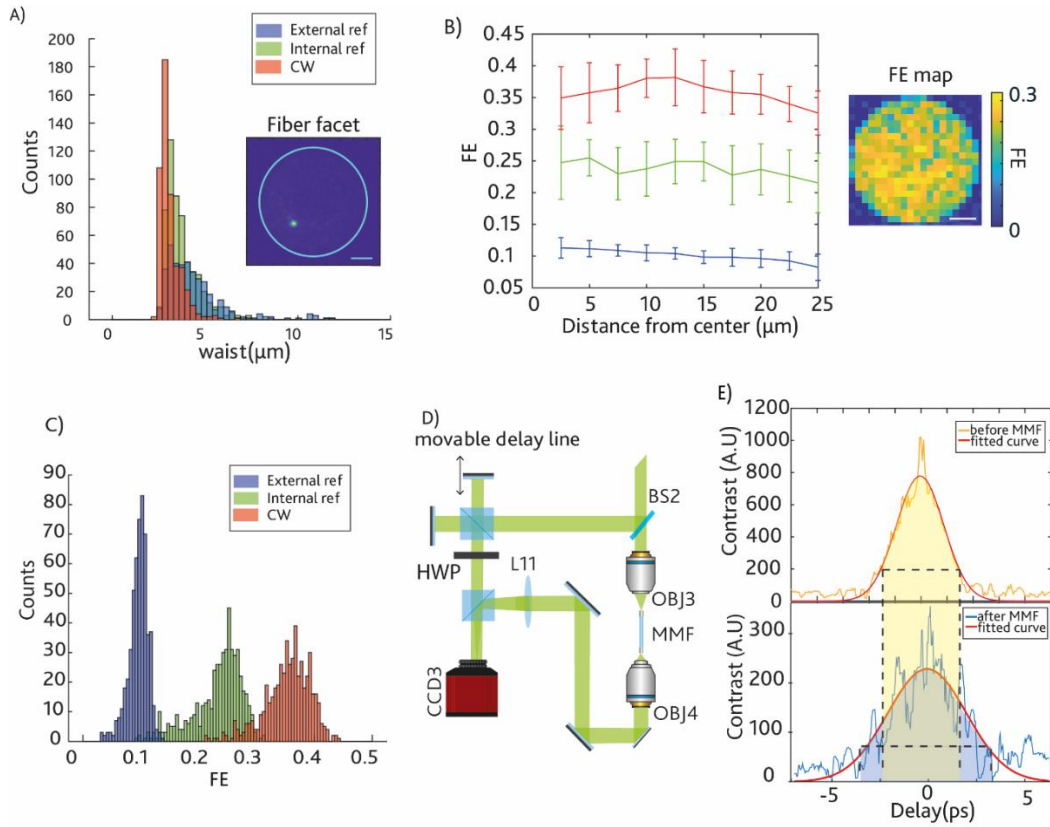


Fig. 2.: A) Waist distribution of focused spot on the fiber output facet. The scale bar represents  $10 \mu\text{m}$ . B) Left: radial distribution of the FE for internal reference CW laser emitting at  $633\text{nm}$  in red, in green internal reference using the SC pulsed laser at  $600\text{nm}$  and external reference in blue. Right: Focusing efficiency map obtained in internal reference configuration using SC pulsed laser. The scale bar represents  $10 \mu\text{m}$ . C) FE distribution obtained with external reference and internal reference using a pulsed source. For comparison, FE distribution obtained with internal reference and CW laser source emitting at  $633 \text{ nm}$  is also presented. D) Optical setup closeup of external reference and autocorrelator path. E) Autocorrelation measures for the beam before the optical fiber and after. The measurement is carried out at  $600 \text{ nm}$ .

### 2.3 Wavelength resilience and chromato-axial volumetric scan

One of the major benefits of employing a pulsed supercontinuum source is the possibility of changing the operational wavelength of the scanning system while preserving coherence. We therefore investigated the properties of the system by calibrating it at either  $\lambda_i = 570, 600$  and  $633 \text{ nm}$ , scanning the output facet of the MMF in  $30 \times 30$  array. In all cases, an internal reference beam was used. The focusing efficiency map at the output facet reveals a similar trend for each employed  $\lambda_i$ , in terms of both FE spatial and intensity distribution (**Figure 3A and 3B**, respectively). Both the average FE and the FE variation as a function of the radial position remain consistent across the three wavelengths (**Figure 3C and 3D**, respectively). On average, across radii and wavelengths,  $\sim 22\%$  of the light is coupled into the focused spot, showcasing the system's resilience across different wavelengths. For an increasing wavelength, the distribution behavior of the waist size is preserved (**Figure 3E**), with the expected waist increase as dictated by the diffraction limit (**Figure 3F**). This is accompanied also by a bigger size as the focused spot moves towards the edge of the fiber core (**Figure 3G**), in agreement with other

literature reports for CW lasers[37]. For the three wavelengths the pulsed speckles experiences similar temporal broadening, as displayed in **Figure 3H** ( $\tau_{570} = 2.1 \pm 0.4$  ps,  $\tau_{600} = 2.6 \pm 0.5$  ps,  $\tau_{633} = 2.7 \pm 0.1$  ps). This confirms that the system performance, in the considered wavelength range, is wavelength resilient upon calibration. Average beam waist and pulse duration obtained at different  $\lambda_i$  are summarized in Table 1.

**Table 1: summary of the different foci parameters obtained at different operational wavelengths.**

Wavelength	Beam waist ( $\pm$ std)	Pulse duration ( $\pm$ std)
570 nm	$4.2 \pm 0.9 \mu\text{m}$	$2.1 \pm 0.4$ ps
600 nm	$4.3 \pm 1.1 \mu\text{m}$	$2.6 \pm 0.5$ ps
633 nm	$4.6 \pm 1.1 \mu\text{m}$	$2.7 \pm 0.1$ ps



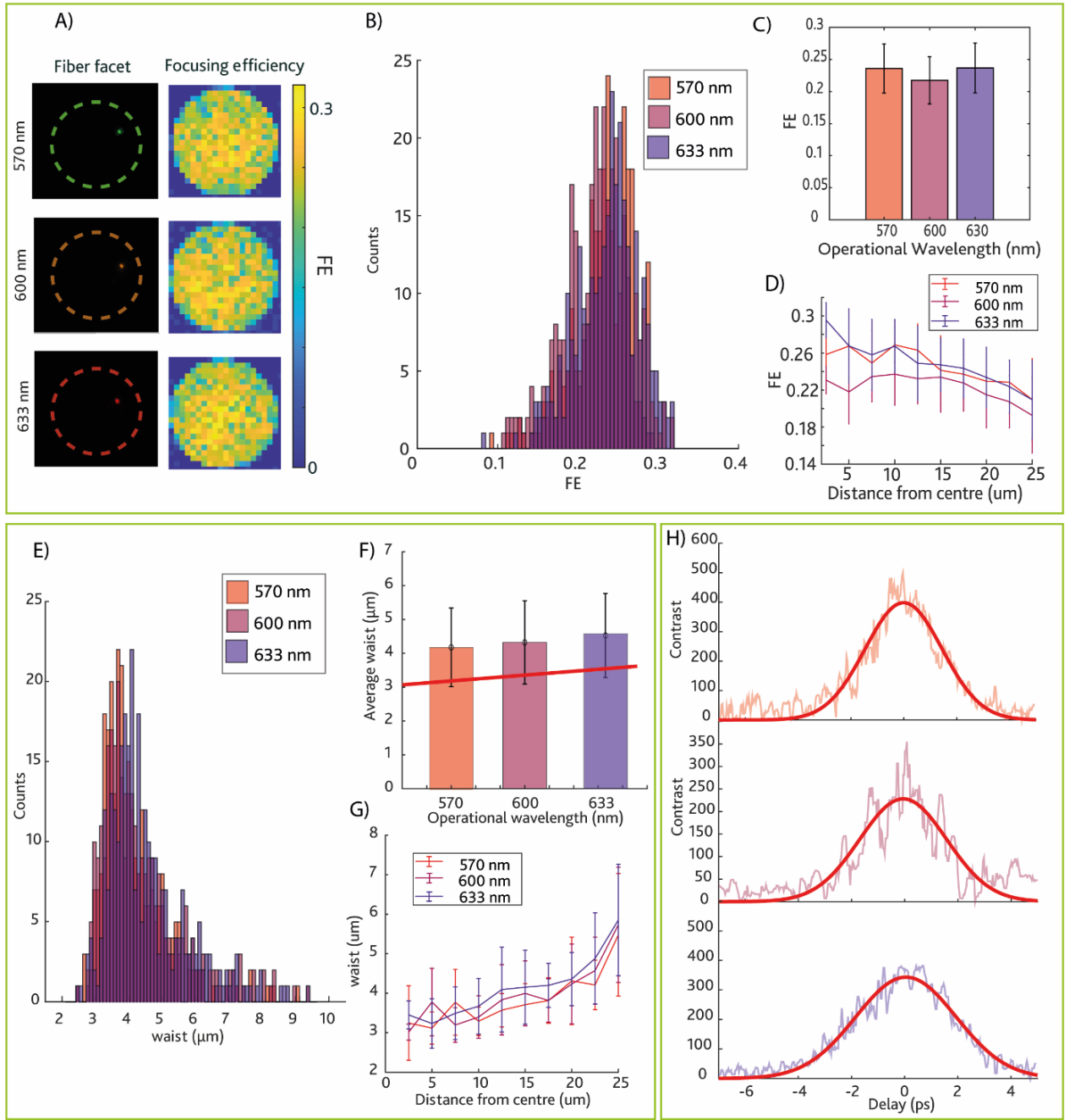


Fig. 3.: A) Foci obtained on the distal facet of the fiber for three operational wavelengths and corresponding focusing efficiency intensity maps. B) Focusing efficiency distribution. C) Average focusing efficiency for the three wavelengths. D) Trend of the focusing efficiency in dependence on the distance from the center of the fiber. E) Waist distributions for  $\lambda_i$ . F) Average waist for the three operational wavelengths. In Red the corresponding diffraction limit for the MMF calculated for  $\lambda_i$ . G) Trend of waist size in dependence on the distance from the center of the fiber. H) Example of temporal measure performed after MMF with Michelson interferometer: in top panel  $\lambda_i = 570 \text{ nm}$ , central panel  $\lambda_i = 600 \text{ nm}$ , bottom panel  $\lambda_i = 633 \text{ nm}$ .

Although switching between different  $\lambda_i$  requires different calibrations, small  $\Delta\lambda$  variations around the central wavelengths enable volumetric scanning by leveraging the chromato-axial memory effect, where the product  $\lambda \cdot z$  (wavelength and axial plane) is conserved[32,38]. To validate this principle for the case of a scanning beam generated through a pulsed internal reference, a calibration at  $\lambda = 600$  nm was performed and a shift of  $\Delta\lambda$  applied afterwards. For  $\lambda + \Delta\lambda = 603$  nm, a shift of the focusing plane of  $\Delta z = -135\mu m$  was observed, as shown in **Figure 4A**. The same procedure can be applied for obtaining a positive  $\Delta z$ : for  $\lambda - \Delta\lambda = 597$  nm, the focusing plane moves by  $\Delta z = +137\mu m$ . This result is consistent with previous findings [38], and it suggests that the system can be employed to perform volumetric scanning (**Figure 4B**). Since the depth of focus was measured to be  $\sim 20\mu m$  (**Figure 4C**), the following characterization of the scanning volume was carried at steps of  $\Delta z = 22.5\mu m$  (which corresponds to  $\Delta\lambda = 0.5$  nm), to assure not overlapped scanning planes (only the case  $\Delta z > 0$  was considered, more relevant for imaging applications). **Figure 4B** displays the focusing efficiency maps over several scanning planes from  $\Delta z = 0$  to  $\Delta z = 112.5\mu m$ , with related histograms in **Figure 4D**. The red circle outlines the effective scanning field (ESF) showing higher and more uniform FE, and outside which distortions of the foci were observed (**Supplementary Video 2**). **Figure 4E** displays the radius of the identified ESF and its average FE as a function of the distance from the fiber facet  $\Delta z$ . Considering the reduction of the FE as a function of depth,  $\Delta z = 90\mu m$  represents an upper limit. Within these limits, the volume available for the scan is a truncated cone of  $V = 8.77 \cdot 10^4 \mu m^3$ . In the volume considered, the average waist size of the focused spot is modified as shown in **Figure 4F**: as the scanning plane moves further from the fiber facet, the waists increase, this is consistent with the angular divergence of the external output modes and with the reduced FE.

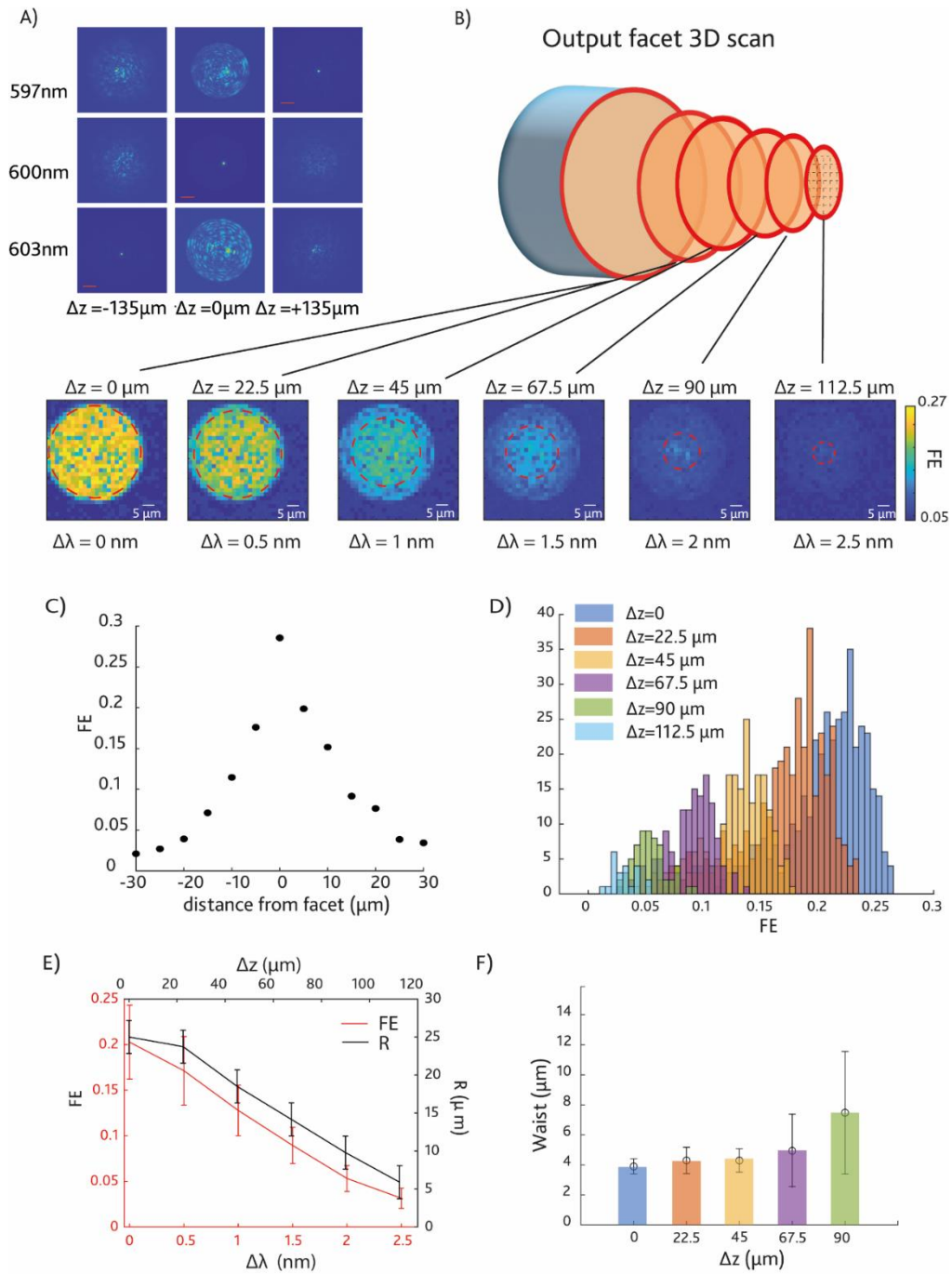


Figure 4: A) Focusing spot at different  $z$  and  $\lambda$ . A shift of  $\pm 3 \text{ nm}$  corresponds to a  $\Delta z = \pm 135 \mu\text{m}$ . The scale bar indicates  $12 \mu\text{m}$ . B) Schematic representation of the scanning volume. For each plane the corresponding FE map is presented. The red circle indicates the area not affected by aberration. The scale bar indicates  $5 \mu\text{m}$ . C) FE dependence on the depth for a fixed focused spot on the fiber facet. The wavelength was set to 600 nm. D) FE distribution at different depths from the fiber facet in the available scanning area. E) Radius of the available scanning area (in black) and average FE in the scanning area (in red) as a function of the average FE depth. F) Average waist of the focused spot at different depths from the fiber facet.

### 3. Discussion and conclusions

We have presented a system for multiplane and multicolor scanning of a supercontinuum source through a MMF, exploiting the advantages of an internal reference beam. The presented data show how this grants a higher focusing efficiency compared to a delayed external reference, with an improvement of 56.4 %. This was obtained while keeping a beam waist close very close to the diffraction limit. In addition, the internal reference approach streamlines the optical setup, which do not require external delay lines. Together with these advantages, the internal reference-based technique comes with two relevant drawbacks: the presence of blind spots due to singularities that prevent a uniform focus on the output facet and the loss of information regarding the phase that gets scrambled along the fiber. While the first problem has been recently solved by implementing a multi-reference calibration [33,39], the second concern still stands but does not impact the possibility to apply the internal reference system in traditional imaging applications.

Since both the reference and the probe beams experience a similar optical path within the MMF, a temporal broadening with respect to the original pulse is observed ( before the fiber  $\tau_{\text{ref}} \sim 1.67 \pm 0.10$  ps, after the fiber  $\tau_{\text{probe}} \sim 2.6 \pm 0.5$  ps). This has to be taken into account when targeting imaging applications requiring pulsed excitation, including FLIM, two-photon microscopy or CARS. In the case of external reference, the delay line acts as a filter selecting only the modes that share similar group velocities preserving the duration of the pulse[30]. If, however, the optimization algorithm is based on the use of an internal reference, most of the modes contribute to the interference since both the reference and the probing mode are decomposed in the internal modes of the fiber and undergo similar dispersion phenomena. While this could limit the use of this system in applications that require extreme temporal control, this is compensated by a much higher focusing efficiency, which is beneficial for applications requiring additional power confined inside the focused spot.

In addition to the temporal behavior characterization, the performances of the internal reference approach are resilient on the choice of the operational wavelength in the calibration process, thereby ensuring a good quality focused spot, in a uniform fashion on the entire core of the fiber, and with a diffraction limited waist for all  $\lambda_i$ . This represents an interesting added benefit for imaging applications where different dyes that operate at different excitation wavelengths are required. Lastly, the chromato-axial memory effect [38] can be employed for moving the scanning plane beyond the fiber facet.

### Acknowledgements

L.C., M.D.V., and Fe.P. acknowledge funding from the European Union's Horizon 2020 Research and Innovation Program under Grant Agreement No. 828972. L.C., M.D.V. and Fe.P. acknowledge funding from the Project "RAISE (Robotics and AI for Socio-economic Empowerment)" code ECS00000035 funded by European Union – NextGenerationEU PNRR MUR - M4C2 – Investimento 1.5 - Avviso "Ecosistemi dell'Innovazione" CUP J33C22001220001. Fi.P., and Fe.P. acknowledge funding from the European Research Council under the European Union's Horizon 2020 Research and Innovation Program under Grant Agreement No. 677683. Fi.P., M.D.V., and Fe.P. acknowledge funding from the European

Union's Horizon 2020 Research and Innovation Program under Grant Agreement No 101016787. M.D.V. acknowledges funding from the European Research Council under the European Union's Horizon 2020 Research and Innovation Program under Grant Agreement No. 692943. M.D.V. acknowledges funding from the U.S. National Institutes of Health (Grant No. U01NS094190). M.D.V., and Fe.P. acknowledge funding from the U.S. National Institutes of Health (Grant No. 1UF1NS108177-01). M.D.V and Fe.P acknowledge funding from European Research Council under the European Union's Horizon 2020 Research and Innovation Program under Grant Agreement No. 966674.

### Conflict of interest

M.D.V. and Fe.P. are founders and hold private equity in Optogenix, a company that develops, produces, and sells technologies to deliver light into the brain.

### References

1. Turtaev, S., Leite, I. T., Altwegg-Boussac, T., Pakan, J. M. P., Rochefort, N. L. and Čižmár, T., "High-fidelity multimode fibre-based endoscopy for deep brain *in vivo* imaging," *Light Sci Appl* **7**(1), 92 (2018).
2. Hayashi, Y., Tagawa, Y., Yawata, S., Nakanishi, S. and Funabiki, K., "Spatio-temporal control of neural activity *in vivo* using fluorescence microendoscopy," *European Journal of Neuroscience* **36**(6), 2722–2732 (2012).
3. Vasquez-Lopez, S. A., Turcotte, R., Koren, V., Plöschner, M., Padamsey, Z., Booth, M. J., Čižmár, T. and Emptage, N. J., "Subcellular spatial resolution achieved for deep-brain imaging *in vivo* using a minimally invasive multimode fiber," *Light Sci Appl* **7**(1), 110 (2018).
4. Zeng, C., Chen, Z., Yang, H., Fan, Y., Fei, L., Chen, X. and Zhang, M., "Advanced high resolution three-dimensional imaging to visualize the cerebral neurovascular network in stroke," *Int J Biol Sci* **18**(2), 552–571 (2022).
5. Weiss, U. and Katz, O., "Two-photon lensless micro-endoscopy with *in-situ* wavefront correction," *Opt Express* **26**(22), 28808 (2018).
6. Accanto, N., Blot, F. G. C., Lorca-Cámara, A., Zampini, V., Bui, F., Tourain, C., Badt, N., Katz, O. and Emiliani, V., "A flexible two-photon fiberscope for fast activity imaging and precise optogenetic photostimulation of neurons in freely moving mice," *Neuron* **111**(2), 176-189.e6 (2023).
7. Choi, W., Kang, M., Hong, J. H., Katz, O., Lee, B., Kim, G. H., Choi, Y. and Choi, W., "Flexible-type ultrathin holographic endoscope for microscopic imaging of unstained biological tissues," *Nat Commun* **13**(1), 4469 (2022).
8. Sattin, A., Antonini, A., Bovetti, S., Moretti, C., Forli, A., Succol, F., Rajamanickam, V., Bertocini, A., Liberale, C. and Fellin, T., "Extended field-of-view microendoscopy through aberration corrected GRIN lenses," *Advances in Microscopic Imaging II*, F. S. Pavone, E. Beaufrepaire, and P. T. So, Eds., 54, SPIE (2019).
9. Cao, H., Čižmár, T., Turtaev, S., Tyc, T. and Rotter, S., "Controlling light propagation in multimode fibers for imaging, spectroscopy and beyond" *Advances in Optics and Photonics* **15**(2), 524-61 (2023).
10. Di Leonardo, R. and Bianchi, S., "Hologram transmission through multi-mode optical fibers," *Opt Express* **19**(1), 247 (2011).
11. Čižmár, T. and Dholakia, K., "Shaping the light transmission through a multimode optical fibre: complex transformation analysis and applications in biophotonics," *Opt Express* **19**(20), 18871 (2011).
12. Collard, L., Pisano, F., Zheng, D., Balena, A., Kashif, M. F., Pisanello, M., D'Orazio, A., de la Prida, L. M., Ciraci, C., Grande, M., De Vittorio, M. and Pisanello, F., "Holographic Manipulation of Nanostructured Fiber Optics Enables Spatially-Resolved, Reconfigurable Optical Control of Plasmonic Local Field Enhancement and SERS," *Small* **18**(23), 2200975 (2022).
13. Papadopoulos, I. N., Farahi, S., Moser, C. and Psaltis, D., "Focusing and scanning light through a multimode optical fiber using digital phase conjugation," *Opt Express* **20**(10), 10583 (2012).
14. Collard, L., Pisano, F., Pisanello, M., Balena, A., De Vittorio, M. and Pisanello, F., "Wavefront engineering for controlled structuring of far-field intensity and phase patterns from multimodal optical fibers," *APL Photonics* **6**(5) (2021).
15. Papadopoulos, I. N., Farahi, S., Moser, C. and Psaltis, D., "High-resolution, lensless endoscope based on digital scanning through a multimode optical fiber," *Biomed Opt Express* **4**(2), 260 (2013).

16. N’Gom, M., Norris, T. B., Michielssen, E. and Nadakuditi, R. R., “Mode control in a multimode fiber through acquiring its transmission matrix from a reference-less optical system,” *Opt Lett* **43**(3), 419 (2018).
17. Li, W., Abrashitova, K., Osnabrugge, G. and Amitonova, L. V., “Generative Adversarial Network for Superresolution Imaging through a Fiber,” *Phys Rev Appl* **18**(3), 034075 (2022).
18. Rahmani, B., Oguz, I., Tegin, U., Hsieh, J., Psaltis, D. and Moser, C., “Learning to image and compute with multimode optical fibers,” *Nanophotonics* **11**(6), 1071–1082 (2022).
19. Collard, L., Kazemzadeh, M., Piscopo, L., De Vittorio, M. and Pisanello, F., “Exploiting holographically end variance to transmit labelled images through a multimode optical fiber,” *Opt Express* (2024).
20. Resisi, S., Popoff, S. M. and Bromberg, Y., “Image Transmission Through a Dynamically Perturbed Multimode Fiber by Deep Learning,” *Laser Photon Rev* **15**(10) (2021).
21. Goel, S., Conti, C., Leedumrongwatthanakun, S. and Malik, M., “Referenceless characterization of complex media using physics-informed neural networks,” *Opt Express* **31**(20), 32824 (2023).
22. Gomes, A. D., Turtaev, S., Du, Y. and Čižmár, T., “Near perfect focusing through multimode fibres,” *Opt Express* **30**(7), 10645 (2022).
23. Stibůrek, M., Ondráčková, P., Tučková, T., Turtaev, S., Šiler, M., Pikálek, T., Jákl, P., Gomes, A., Krejčí, J., Kolbábková, P., Uhlířová, H. and Čižmár, T., “110  $\mu\text{m}$  thin endo-microscope for deep-brain in vivo observations of neuronal connectivity, activity and blood flow dynamics,” *Nat Commun* **14**(1), 1897 (2023).
24. Li, W., Abrashitova, K. and Amitonova, L. V., “Super-resolution multimode fiber imaging with an untrained neural network,” *Opt Lett* **48**(13), 3363 (2023).
25. Stellinga, D., Phillips, D. B., Mekhail, S. P., Selyem, A., Turtaev, S., Čižmár, T. and Padgett, M. J., “Time-of-flight 3D imaging through multimode optical fibers,” *Science* (1979) **374**(6573), 1395–1399 (2021).
26. Morales-Delgado, E. E., Psaltis, D. and Moser, C., “Two-photon imaging through a multimode fiber,” *Opt Express* **23**(25), 32158 (2015).
27. Pedretti, E., Tanner, M. G., Choudhary, T. R., Krstajić, N., Megia-Fernandez, A., Henderson, R. K., Bradley, M., Thomson, R. R., Girkin, J. M., Dhaliwal, K. and Dalgarno, P. A., “High-speed dual color fluorescence lifetime endomicroscopy for highly-multiplexed pulmonary diagnostic applications and detection of labeled bacteria,” *Biomed Opt Express* **10**(1), 181 (2019).
28. Trägårdh, J., Pikálek, T., Šerý, M., Meyer, T., Popp, J. and Čižmár, T., “Label-free CARS microscopy through a multimode fiber endoscope,” *Opt Express* **27**(21), 30055 (2019).
29. Cifuentes, A., Pikálek, T., Ondráčková, P., Amezúa-Correa, R., Antonio-Lopez, J. E., Čižmár, T. and Trägårdh, J., “Polarization-resolved second-harmonic generation imaging through a multimode fiber,” *Optica* **8**(8), 1065 (2021).
30. Morales-Delgado, E. E., Farahi, S., Papadopoulos, I. N., Psaltis, D. and Moser, C., “Delivery of focused short pulses through a multimode fiber,” *Opt Express* **23**(7), 9109 (2015).
31. Velsink, M. C., Amitonova, L. V. and Pinkse, P. W. H., “Spatiotemporal focusing through a multimode fiber via time-domain wavefront shaping,” *Opt Express* **29**(1), 272 (2021).
32. Čižmár, T. and Dholakia, K., “Exploiting multimode waveguides for pure fibre-based imaging,” *Nat Commun* **3**(1), 1027 (2012).
33. Collard, L., Piscopo, L., Pisano, F., Zheng, D., De Vittorio, M. and Pisanello, F., “Optimizing the internal phase reference to shape the output of a multimode optical fiber,” *PLoS One* **18**(9), e0290300 (2023).
34. Pikálek, T., Trägårdh, J., Simpson, S. and Čižmár, T., “Wavelength dependent characterization of a multimode fibre endoscope,” *Opt Express* **27**(20), 28239 (2019).
35. Alfano, R. R., ed., [The Supercontinuum Laser Source, Second Edition], Springer-Verlag, New York (2006).
36. Schmidt, C. C., Turcotte, R., Booth, M. J. and Emptage, N. J., “Repeated imaging through a multimode optical fiber using adaptive optics,” *Biomed Opt Express* **13**(2), 662 (2022).
37. Descloux, A., Amitonova, L. V. and Pinkse, P. W. H., “Aberrations of the point spread function of a multimode fiber due to partial mode excitation,” *Opt Express* **24**(16), 18501 (2016).
38. Devaud, L., Guillon, M., Gusachenko, I. and Gigan, S., “Chromato-axial memory effect in step-index multimode fibers,” *APL Photonics* **6**(12), 126105 (2021).
39. Jákl, P., Šiler, M., Ježek, J., Cifuentes, Á., Trägårdh, J., Zemánek, P. and Čižmár, T., “Endoscopic Imaging Using a Multimode Optical Fibre Calibrated with Multiple Internal References,” *Photonics* **9**(1), 37 (2022).